Monthly Notices of the ROYAL ASTRONOMICAL SOCIETY

MNRAS **527,** 5717–5731 (2024)
Advance Access publication 2023 November 14

https://doi.org/10.1093/mnras/stad3505

Multiwavelength observations of the lensed quasar PKS 1830-211 during the 2019 γ-ray flare

S. Vercellone [1★] I. Donnarumma,[2] C. Pittori [3,4] F. Capitanio,[5] A. De Rosa [5] L. Di Gesu,[2] S. Kiehlmann [6,7] M. N. Iacolina,[2] P. A. Pellizzoni,[8] E. Egron [8] L. Pacciani,[5] G. Piano,[5] S. Puccetti,[2] S. Righini,[9] G. Valente,[2] F. Verrecchia [3,4] V. Vittorini,[5] M. Tavani,[5] E. Brocato,[3,10] A. W. Chen [11] T. Hovatta,[12,13] A. Melis,[8] W. Max-Moerbeck [14] D. Perrodin,[8] M. Pilia,[8] M. Pili,[8] A. C. S. Readhead,[15] R. Reeves [16] A. Ridolfi [8] F. Vitali,[3] A. Bulgarelli,[17] P. W. Cattaneo,[18] F. Lucarelli,[3,4] A. Morselli[19] and A. Trois [8]

Affiliations are listed at the end of the paper

Accepted 2023 November 9. Received 2023 November 9; in original form 2023 May 17

ABSTRACT

PKS 1830-211 is a γ-ray emitting, high-redshift (z =2.507 $\pm$ 0.002), lensed flat-spectrum radio quasar. During the period 2019 mid-February to mid-April, this source underwent a series of strong γ-ray flares that were detected by both AGILE-GRID (Gamma-Ray Imaging Detector) and *Fermi* Large Area Telescope (*Fermi*-LAT), reaching a maximum γ-ray flux of $F_{\rm E>100\,MeV} \approx 2.3 \times 10^{-5}$ photons cm^{-2} s^{-1}. Here, we report on a coordinated campaign from both on-ground [Medicina, Owens Valley Radio Observatory (OVRO), Rapid Eye Mount (REM), and Sardinia Radio Telescope (SRT)] and orbiting facilities (AGILE, *Fermi*, *INTEGRAL*, *NuSTAR*, *Swift*, and *Chandra*), with the aim of investigating the multiwavelength properties of PKS 1830-211 through nearly simultaneous observations presented here for the first time. We find a possible break in the radio spectra in different epochs above 15 GHz, and a clear maximum of the 15 GHz data approximately 110 d after the γ-ray main activity periods. The spectral energy distribution shows a very pronounced Compton dominance ($>$ 200) which challenges the canonical one-component emission model. Therefore, we propose that the cooled electrons of the first component are re-accelerated to a second component by, for example, kink or tearing instability during the γ-ray flaring periods. We also note that PKS 1830-211 could be a promising candidate for future observations with both Compton satellites [e.g. enhanced ASTROGAM (e-ASTROGAM)] and Cherenkov arrays [Cherenkov Telescope Array Observatory (CTAO)] which will help, thanks to their improved sensitivity, in extending the data availability in energy bands currently uncovered.

Key words: acceleration of particles – radiation mechanisms: non-thermal – relativistic processes – quasars: individual: PKS 1830-211 – quasars: supermassive black holes – gamma rays: galaxies.

1 INTRODUCTION

PKS 1830-211 is a high-redshift blazar ($z = 2.507 \pm 0.002$, Lidman et al. 1999) that is gravitationally lensed by a spiral galaxy at $z = 0.886$ (Wiklind & Combes 1996), as shown by the two radio lobes located 1 arcsec apart from each other (A e B components, Lovell et al. 1998). The lensed counterparts were also observed in the near-infrared (NIR) and optical energy bands by the *Hubble Space Telescope* and the Gemini Observatory (Courbin et al. 2002). The source was observed in X-rays by both *XMM–Newton* and *Chandra*, enabling for a study of the complex soft X-ray behaviour in detail (De Rosa et al. 2005; Dai et al. 2008). PKS 1830-211 is a well-known γ-ray source above 100 MeV, identified as such by Mattox et al. (1997) and subsequently listed in both the AGILE (Verrecchia et al. 2013; Bulgarelli et al. 2019) and *Fermi*-LAT (Abdollahi et al. 2020) catalogues, which has produced several γ-ray flares over the last two decades (Hartman et al. 1999; Donnarumma et al. 2011; Abdo et al. 2015). A quite bright γ-ray flare was detected by AGILE and *Fermi*-LAT in 2010 October–November, and multiwavelength observations were carried out, as reported in Donnarumma et al. (2011) and Abdo et al. (2015). The multiwavelength campaign carried out in 2010 with AGILE (Donnarumma et al. 2011) showed that the intense γ-ray flare had no significant counterpart at lower frequencies, making this blazar classified as a 'γ-ray only flaring blazar'. This behaviour was discussed according to both (macro/micro) lensing and intrinsic physical properties of the blazar. In particular, macro- and microlensing were excluded, given the chromaticity of the flare and the time-scale of the γ-ray variability (Donnarumma et al. 2011). The flare was therefore associated with intrinsic variations of the jet emission, which are difficult to be interpreted in the one zone leptonic model (Ghisellini, Maraschi & Treves 1985) given the high Compton dominance (i.e. the ratio of the peak of the Compton to the synchrotron peak luminosities) of the typical

★ E-mail: stefano.vercellone@inaf.it

two-bump spectral energy distribution (SED) in flat-spectrum radio quasars. Alternative models have been invoked to overcome the limits of the one-zone leptonic models, such as the 'mirror model' (Tavani, Vittorini & Cavaliere 2015; Vittorini, Tavani & Cavaliere 2017) or the 'jet-cloud interaction model' (Araudo, Bosch-Ramon & Romero 2010; Vittorini et al. 2014). A long term γ-ray monitoring program represents an optimal tool to search for the time delay between the emissions of the two lensed images A and B as measured in the radio maps (26^{+4}_{-5} d, Lovell et al. 1998).

AGILE did not detect any delay between the lensed components during the γ-ray activity recorded in 2010 October–November, which would infer a lack of delay if the flux ratio of the two components is ∼1, as observed in radio (no conclusion could be drawn if this value was below 1 due to the AGILE sensitivity). The missing evidence of an echo can be explained with a flux ratio of the two components not equal to 1 in γ-rays. The dependence on energy of the flux ratio of the two components can be explained by invoking microlensing effects (Blackburne, Pooley & Rappaport 2006; Donnarumma et al. 2011; Abdo et al. 2015). Further analyses of the γ-ray light curve with a larger sensitivity were performed by Abdo et al. (2015). By scanning a longer period (2008 August–2011 July), two large γ-ray flares of PKS 1830-211 were detected by *Fermi*-LAT with no evidence for a delayed activity. Nevertheless, Abdo et al. (2015) were able to place a lower limit of ∼ 6 on the flux ratio between the two lensed images. Barnacka et al. (2015), analysing *Fermi*-LAT data between 2008 August and 2015 January found a γ-ray time-delay consistent with the radio one, while Abhir et al. (2021), analysing a time period in 2019 similar to the one discussed in this paper, found no clear evidence of such a γ-ray time delay.

In this paper, we present the multifrequency campaign on PKS 1830-211 during the period 2019 mid-February to mid-April and involving measurements in the radio, NIR, optical, ultraviolet (UV), X-ray, and γ-ray energy bands. The paper is organized as follows. Section 2 reports on the different facilities involved in this observing campaign. In Section 3, we discuss our results, while in Appendices A–D we report the multiwavelength observations. We adopt a lambda-cold dark matter cosmology (Planck Collaboration VI 2020) with the following parameters $H_0 = 67.7$, $\Omega_m = 0.31$, and $\Omega_\Lambda = 0.69$.

2 SUMMARY OF OBSERVATIONS AND FLARE DEFINITION

The detection of γ-ray flares from PKS 1830 -211 triggered a large multiwavelength observing campaign, involving both on-ground [Medicina, Owens Valley Radio Observatory (OVRO), REM, and Sardinia Radio Telescope (SRT)] and orbiting facilities (AGILE, *Fermi*, *INTEGRAL*, *NuSTAR*, *Swift*, and *Chandra*).

Fig. 1 shows the multiwavelength coverage as a function of time of the different instruments, while Table 1 reports the different energies covered by our campaign. These observations allow us to reconstruct an almost simultaneous SED spanning about 15 decades in energy. The detailed description of each facility, data reduction, data analysis, and the presentation of the results can be found in Appendix A (γ-ray data), Appendix B (X-ray data), Appendix C (IR, optical, and UV data), and Appendix D (radio data). The *Fermi*-LAT 12-h binning allows us to obtain a detailed description of the different γ-ray flares. We anticipate here the method we used for selecting the different γ-ray flares time intervals.

'Unbinned light curves' were produced for the brightest flaring periods following the procedure described in Pacciani (2018), by means of a photometric method. Gamma-rays are collected within

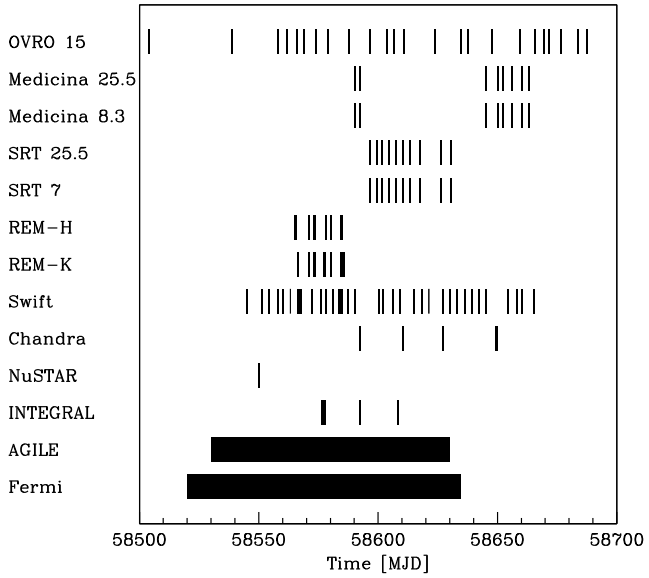

Figure 1. Coverage of the different facilities as a function of time. The first five values in the ordinate label refer to the observing frequency in GHz.

Table 1. List of facilities and their energy range.

Facility	Energy/ wavelength/ frequency
Fermi-LAT	0.1–300 GeV
AGILE-GRID	0.1–30 GeV
INTEGRAL-ISGRI	13–200 keV
NuSTAR	3–78.4 keV
Chandra-ACIS	0.5–8 keV
Swift-XRT	0.3–10 keV
Swift-UVOT	*v* 5468 Å
	b 4392 Å
	u 3465 Å
	w1 2600 Å
	m2 2246 Å
	w2 1928 Å
REM-REMIR	*K* 22000 Å
REM	*H* 16350 Å
SRT	*C*-band 7 GHz
	K-band 25.5 GHz
Medicina	*X*-band 8.3 GHz
	K-band 25.5 GHz
OVRO	15 GHz

an extraction region of radius $R^i_{68\ \%}(E)$ that varies with the energy and type of the reconstructed γ-ray. $R^i_{68\ \%}(E)$ corresponds to the 68 % containment radius of γ-rays of energy E and reconstruction topology PSF_i (point-spread function, with $i = 1,..., 4$). A novel method to select flares within a set of time-tagged data has been used. It is a clustering method (iSRS, iterated short range search) in one dimension (the cumulative exposure domain), followed by a statistical discrimination based on maximum-score scan statistics (Glaz & Zhang 2006). Once the set of collected γ-rays are produced, a clustering scheme in the cumulative exposure domain is performed. Maximum-score scan statistics is applied to remove statistically not-relevant clusters (see Pacciani 2018, for details). The threshold chance probability to discriminate non-relevant clusters is set to 1.3‰. The set of remaining clusters is a root, with leaves

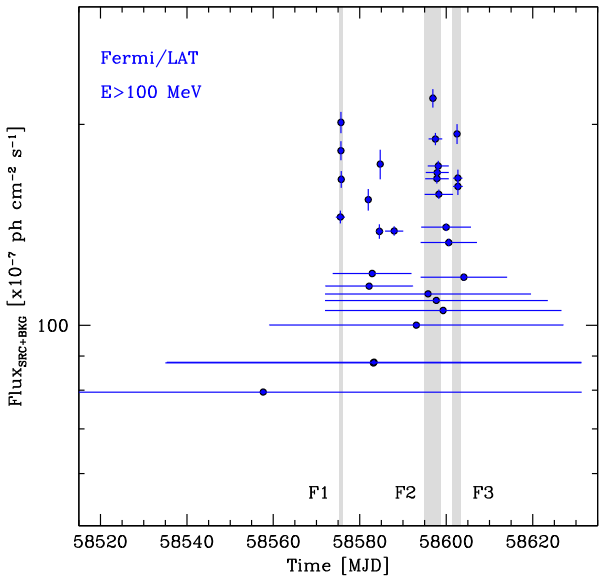

Figure 2. PKS 1830 -211 *Fermi*-LAT unbinned light curve (a data clustering following Pacciani 2018). The most significant flares (and their durations) are reported as dashed areas. Background contribution is not subtracted. Dashed vertical bands correspond, from left to right, to F1, F2, and F3, respectively.

Table 2. *Fermi*-LAT spectral properties during the different flaring periods.

Period	$F_{E>100\,MeV}$ (10^{-5} photons cm^{-2} s^{-1})	α	β
F1	1.95 ± 0.07	2.44 ± 0.05	0.11 ± 0.03
F2	2.07 ± 0.07	2.26 ± 0.03	0.15 ± 0.02
F3	1.77 ± 0.07	2.33 ± 0.03	0.12 ± 0.02
4FGL	$(4.47 \pm 0.12) \times 10^{-2}$	2.46 ± 0.01	0.09 ± 0.01

corresponding to the detected peaks. Each cluster can be described by its mean time, the average flux within the cluster, and its length in time domain. In Fig. 2, we show the set of remaining clusters (represented by a segment) for PKS 1830 − 211. We call this set the unbinned light curve. The most significant flares are F1 (MJD 58575.2 − 58576.1), F2 (MJD 58595.0 − 58598.8), and F3 (MJD 58601.5 − 58603.4). Table 2 shows the *Fermi*-LAT spectral properties during the different flaring periods, assuming a log-parabola model,

$$\frac{dN}{dE} = K_0 \left(\frac{E}{E_0}\right)^{-\alpha-\beta\ln(E/E_0)}, \quad (1)$$

where α is the spectral slope, and β the curvature. The last value refers to the *Fermi* Fourth Point Source (4FGL) Catalogue one.

3 RESULTS AND DISCUSSION

3.1 Multiwavelength data

Fig. 3 shows the PKS 1830 -211 multiwavelength light curves. From top to bottom, we show the radio (OVRO 15 GHz, Medicina 8.3 and 25.5 GHz, and SRT 7 and 25.5 GHz), IR (REM *H* and *K* bands), X-ray (*Swift*/X-ray Telescope, XRT and *Chandra*), and γ-ray (AGILE-GRID, Gamma-Ray Imaging Detector and *Fermi*-LAT) data, respectively. The source reached its maximum flux ($F_{E>100\,MeV} = (2.28 \pm 0.25) \times 10^{-5}$ photons cm^{-2} s^{-1}) around April 24 (MJD=58597.25 ± 1.0), as shown in panel (d). This flux level is unprecedented for this source, and it is one of the largest ever detected in γ-rays from blazars at redshift $z > 2$ (see Vercellone et al. 2019, for 4C+71.07 at $z = 2.172$). Our *Chandra* data show that the flux is somewhat higher than what reported in De Rosa et al. (2005) for the *Chandra* observations of 2000–2001 and we also find an intervening column density $N_{H,\,lens}$ slightly higher than what found in De Rosa et al. (2005). To further investigate the possible variability of the spectral parameters of the source, we compared the count-rate observed in the two lensed images of PKS 1830-211 in a soft (0.5–2.0 keV) and in a hard (2.0–8.0 keV) energy band, as shown in Fig. B2. In the last two shorter observations, the ratio is unconstrained in the soft band. A slight decrease of the ratio N/S is observed, in agreement with that reported in Wilms et al. (2019) for the ObsID 22197−22198. The decrease is more noticeable in the soft X-ray domain, which suggests variability of the absorbing column density in the lensing galaxy. However, higher quality, spatially resolved X-ray data would be needed to draw firm conclusions.

Fig. 4 shows the OVRO 15 GHz light curve starting from 2018 mid-October to 2020 mid-February. The vertical grey bands mark the time interval of the γ-ray flares. The light-curve shows the increasing trend of the 15 GHz flux during the γ-ray observations. This Figure clearly shows how the maximum of the 15 GHz emission occurs about 110 d after the major γ-ray activity period, followed by a decay (∼4 Jy) in 100 d at a radio flux level comparable with the one at the onset of γ-ray flares. Pushkarev, Kovalev & Lister (2010) found that there is a delay between the γ-ray and the radio emission (the γ-ray emission leads the radio one) up to eight months in the observer's frame (an average of one month in the rest frame). According to Pushkarev et al. (2010), this evidence can be explained by the synchrotron opacity in the nuclear region. Our results, for $z = 2.507$, are perfectly in agreement with this scenario.

Fig. 3, panel (a) shows the SRT/Medicina radio light curve for the three frequency bands observed: *K* band (25.5 GHz) is indicated in red for both telescopes; *X* band (8.3 GHz) in blue, and *C* band (7 GHz) in green. Data are reported in Table D1. The *K*-band light curve displays a slight decrease in the observed time range, while lower frequency data seem to show a weak rise, although a clear trend is not evident and a short-term variability is detected. Therefore, a slight spectral break seems to manifest in the 56620−56640 MJD range. As the increasing flux density trend shown by OVRO data at 15 GHz has extended over about 58700 MJD (see Fig. 4), the observed spectral break is likely to occur in the 15–26 GHz range. This break is clearly visible when analysing the SRT and Medicina radio spectra shown in Fig. 5: a clear break emerges, with a decrease of the flux density at the highest frequency in the observed time range. This is a typical behaviour observed during the course of a flare for extragalactic jetted sources, which can undergo oscillations and variability of the radio flux density on week/month time-scale, in a non-synchronous way at the several radio frequencies (see e.g. Fromm et al. 2011).

Fig. 6 shows the *Fermi*-LAT 12-h bin ($E > 300$ MeV) photon index as a function of the 12-h bin flux during the three main γ-ray flares F1, F2, and F3. It is worth noting that all the flares show the same achromatic behaviour, that is, the photon index remains almost constant when the flux increases by a factor greater than 5. The average values of the γ-ray photon indices during the three different flares are $\Gamma_{F1} = 2.58 \pm 0.07$, $\Gamma_{F2} = 2.45 \pm 0.04$, and $\Gamma_{F3} = 2.50 \pm 0.06$. These values are in agreement with the one reported in Abdo et al. (2010), $\Gamma = 2.46 \pm 0.18$, for flat-spectrum radio quasars (FSRQs), as well as the low scatter as a function of the increasing flux. As noted by Abdo et al. (2010), the low dispersion observed may support the idea that a very limited number of physical

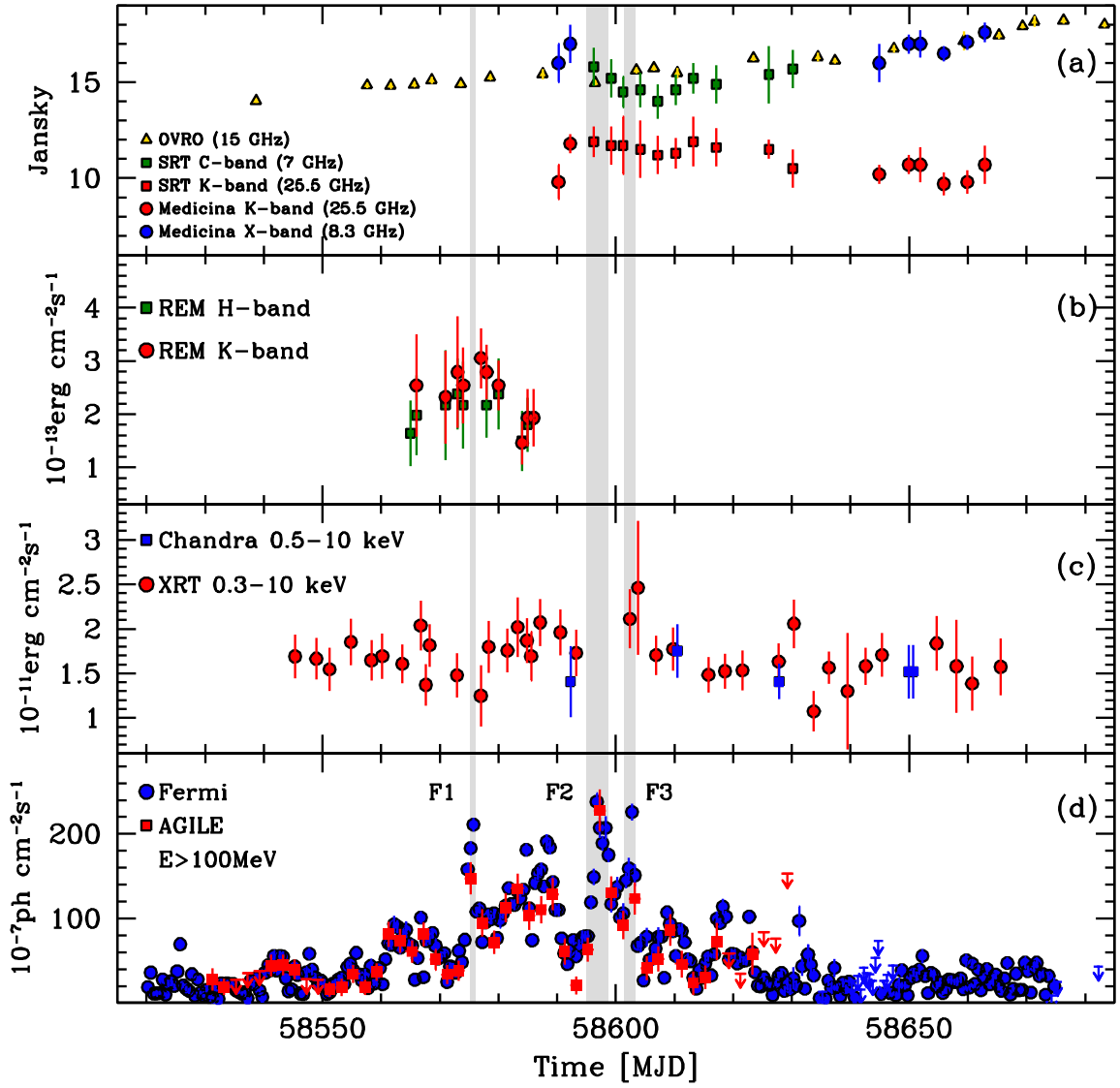

Figure 3. PKS 1830-211 multiwavelength light curves. From top to bottom: radio (7, 8.3, 15, 25.5) GHz, IR (*H* and *K* bands), X-ray (0.3–10) keV, and γ-ray ($E > 100$ MeV) data. The dashed areas correspond to the major γ-ray flares F1, F2, and F3, when the SEDs were computed. Arrows mark 3σ upper limits.

parameters drive the spectrum shape in the GeV energy range and that it can also be connected to distinct dominant emission mechanisms, for example, external Compton for FSRQs.

The 12-h binning of the *Fermi*-LAT γ-ray light curve allows us evaluate the fractional variability and its uncertainty,

$$F_{\rm var} = \sqrt{\frac{S^2 - \bar{\sigma^2}}{\bar{x}^2}} \pm \sqrt{\left(\sqrt{\frac{1}{2N}}\frac{\bar{\sigma}^2_{\rm err}}{\bar{x}^2 F_{\rm var}}\right)^2 + \left(\sqrt{\frac{\bar{\sigma}^2_{\rm err}}{N}}\frac{1}{\bar{x}}\right)^2}, \quad (2)$$

according to formulae (10) and (B2) in Vaughan et al. (2003). We computed $F_{\rm var}$ for both $E > 100$ and > 300 MeV in the period MJD 58520–58680, in order to check for any possible dependence of the variability on the energy threshold, obtaining $F_{\rm var}^{\rm E>100MeV} = 0.842 \pm 0.007$ and $F_{\rm var}^{\rm E>300MeV} = 0.723 \pm 0.015$, respectively. These results show a slightly enhanced variability when considering the lower energy threshold with respect to the higher one. We also computed $F_{\rm var}$ for the data at other frequencies. Only AGILE-GRID ($E > 100$ MeV), *Swift*-XRT (0.3–10 keV), and OVRO (15 GHz) data yield non-null $F_{\rm var}$ values: $F_{\rm var}^{\rm AGILE} = 0.62 \pm 0.04$, $F_{\rm var}^{\rm XRT} = 0.09 \pm 0.05$, and $F_{\rm var}^{\rm OVRO} = 0.078 \pm 0.003$, respectively. We note that, as seen in other blazars (e.g. 3C 454.3, Vercellone et al. 2010), $F_{\rm var}$ is higher in the γ-ray energy band than in the radio band. We should also consider that the calculation of $F_{\rm var}$ could be influenced both by the binning of the light curve and by the source coverage at different frequencies, as discussed in detail in Schleicher et al. (2019).

We can also estimate the minimum variability time-scale for $E > 100$ MeV by analysing the 12-h-binned *Fermi*-LAT light curve, $t_{\rm var} = \ln(2) \times \tau_{\rm d}$ d, where $\tau_{\rm d}$ is the doubling (R, rising portion of the light curve)/halving (D, decaying portion of the light curve) time defined by

$$F(t_2) = F(t_1) \times 2^{(t_2 - t_1)/\tau_{\rm d}}, \quad (3)$$

and $F(t_1)$ and $F(t_2)$ are the $E > 100$ MeV γ-ray fluxes at the times t_1 and t_2, respectively. The AGILE-GRID γ-ray data have a much larger binning (48 h) compared with the *Fermi*-LAT one (12 h), which makes the AGILE data less constraining to assess time variability on short time-scales. Table 3 shows the minimum doubling/halving times and their significance, $\sigma(\tau_{\rm d}) = |F(t_1) - F(t_2)|/\sigma(F(t_1))$. We

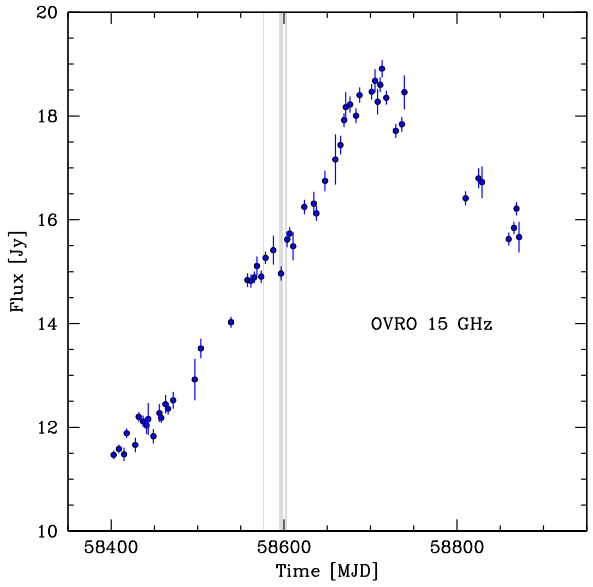

Figure 4. OVRO 15 GHz light curve. The grey vertical bands mark the different γ-ray flares.

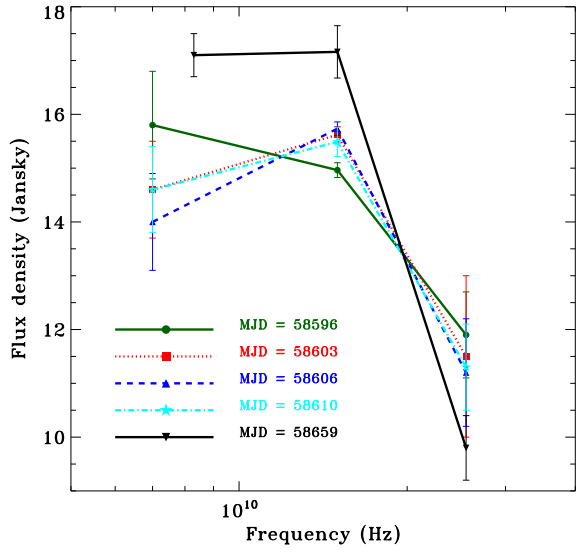

Figure 5. PKS 1830-211 radio spectra at different epochs. We include data from Medicina, OVRO, and SRT telescopes at 7, 8.3, 15, and 25.5 GHz. The spectral points were integrated into period ranges whose MJD reference is indicated in the figure.

selected those doubling/halving times with $\sigma(\tau_d) \geq 3$. Assuming $\tau_d = \min\{\tau_d(R); \tau_d(D)\}$, we obtain the minimum variability timescale $t_{var} = 0.15$ d.

This quantity can be used to derive the minimum Doppler factor (Dondi & Ghisellini 1995),

$$\delta_{min} \geq \left[3.5 \times 10^3 \frac{(1+z)^{2\alpha}(1+z-\sqrt{1+z})^2 F_x (3.8\nu_\gamma \nu_x)^\alpha}{t_{var}}\right]^{1/(4+2\alpha)}, \quad (4)$$

where z is the source redshift, α is the energy spectral index in the X-ray band, F_x is the X-ray flux at 1 keV in μJy, ν_γ is the average energy of the maximum energy bin in GeV of the γ-ray spectrum, and ν_x is 1 keV. In order to derive the X-ray flux and spectral properties,

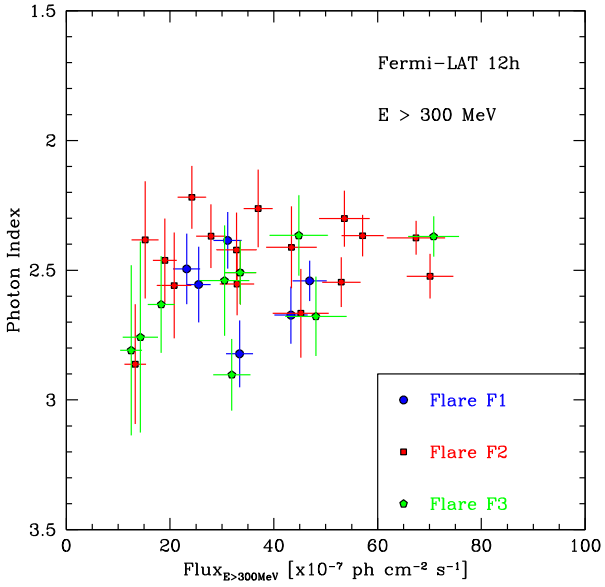

Figure 6. *Fermi*-LAT 12-h bin ($E > 300$ MeV) photon index as a function of the 12-h bin flux during the three main γ-ray flares F1, F2, and F3.

we stacked all the *Swift*/XRT observations, because of their moderate variability. We obtain $F_{0.3-10\,keV} = (1.65^{+0.04}_{-0.04}) \times 10^{-11}$ erg cm^{-2} s^{-1} and $\alpha = 1.32^{+0.06}_{-0.05}$, which yields $\delta_{min} \geq 24.3$.

3.2 Spectral energy distribution

During our observing campaign we collected multiwavelength data covering the main γ-ray flares. Fig. 7 shows the PKS 1830- 211 SED. In the radio and IR energy bands, points and colours follow those presented in Fig. 3. Purple upper limits represent the *Swift*/UVOT data, integrated during the whole observing campaign. In the X-ray energy band, cyan and red points represent *Swift*/XRT spectra accumulated on MJD 58568–58578 (γ-ray F1) and MJD 58590–58606 (γ-ray F2+F3), respectively. Blue points represent *NuSTAR* data acquired on MJD 58550, while golden points are the sum of all the *INTEGRAL*/IBIS (Imager on Board the Integral Satellite) observations. The combined X-ray spectral model fitting was performed with the following parameters: `const*phabs*(zphabs*pow)` fixing the absorption along the line of sight to $N_H^{gal} = 0.187 \times 10^{22}$ cm^{-2} and $N_H^{lens} = 3.1 \times 10^{22}$ cm^{-2} (assuming $z_{lens} = 0.89$). Both fits yield a photon index of 1.46 ± 0.01.

In the γ-ray energy band, we investigated the *Fermi*-LAT finer time-binning in order to select the most significant flare episodes, F1, F2, and F3. The corresponding AGILE-GRID photon indices are $\Gamma(F1) = 2.35 \pm 0.14$, $\Gamma(F2) = 2.29 \pm 0.09$, and $\Gamma(F3) = 2.00 \pm 0.16$, respectively. Small grey points are archival data provided by the ASI Space Science Data Centre (ASI/SSDC) *SED Builder Tool* (Stratta et al. 2011) which include public catalogues and surveys. The data show the typical double-humped shape of the blazar SED. Moreover, while the rising branch of the inverse Compton (IC) and the poorly constrained synchrotron emission are almost consistent with the previous SEDs, the high-energy peak ($E > 100$ MeV) is about a factor of 3–4 more intense with respect to the flare discussed in Donnarumma et al. (2011), whose SED fits are reported as dotted line (quiescent state), dashed line (one-month integration around the 2010 flare) and dotted–dashed line (5-d flare).

We model the flare F1 for which we have simultaneous data in radio, IR, optical, X-ray and γ-ray bands (IR data are relevant to

Table 3. Minimum doubling (R, rising portion of the light curve) and halving (D, decaying portion of the light curve) time τ_d.

t_1 (MJD)	t_2 (MJD)	$F(t_1)$ (10^{-7}photons cm^{-2} s^{-1})	$F(t_2)$ (10^{-7}photons cm^{-2} s^{-1})	τ_d (d)	Doubling/halving raise/decay	Significance ($\sigma(\tau_d)$)
58539.75	58540.25	6.9 ± 1.9	36.0 ± 4.6	0.21	R	15.3
58527.75	58528.25	34.0 ± 4.6	8.2 ± 1.9	0.25	D	5.6

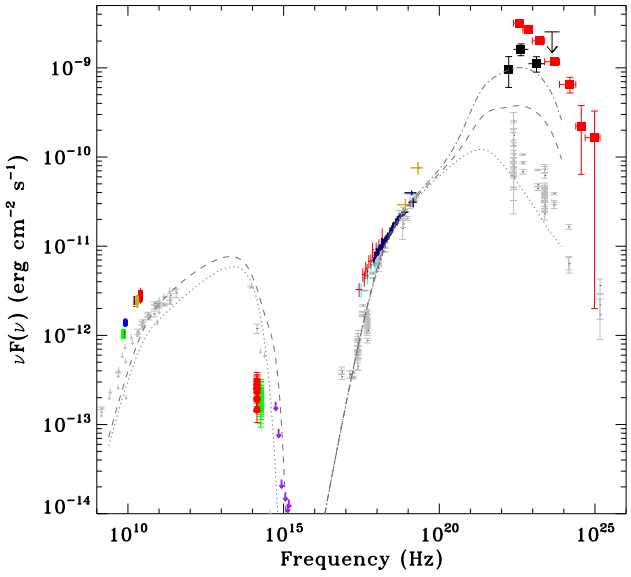

Figure 7. PKS 1830-211 SEDs for the three major γ-ray flares (see Section 3.2 for details). In the radio band, green, blue, golden, and red points represent 7, 8.3, 15, and 25.5 GHz data. In the IR band, green and red points represent REM-*H* and REM-*K* bands, respectively. Purple upper limits represent the *Swift*/UVOT data, integrated during the whole observing campaign. In the X-ray energy band, cyan and red points represent *Swift*/XRT spectra accumulated on MJD 58568–58578 (γ-ray F1) and MJD 58590–58606 (γ-ray F2+F3), respectively. Blue points represent *NuSTAR* data acquired on MJD 58550, while golden points are the sum of all the *INTEGRAL*/IBIS observations. For sake of clarity, in the γ-ray energy band, we report data pertaining to flare F1. Red filled squares correspond to *Fermi*-LAT F1 data, while black filled squares correspond to AGILE-GRID data acquired on a similar period. Small grey points are archival data. The dotted, dashed, and dotted–dashed dark grey lines correspond to the 2010 SEDs for the average γ-ray state, the 1-month integration, and the 5-d γ-ray flare, respectively, as described in Donnarumma et al. (2011).

constrain the synchrotron component). The data show very high Compton dominance, with stronger daily variability in γ-rays than the others bands: these data challenge a simple one-zone model (see e.g. Vittorini et al. 2017). Adapting the original model discussed in Vittorini et al. (2009), we first consider the emission in optical–UV. Assuming a magnification factor due to gravitational lensing of the order of 10 (see e.g. Donnarumma et al. 2011), the accretion disc has to radiate $L_{\rm d} \lesssim 10^{45}$ erg s^{-1}at blackbody temperature $T_{\rm d} \approx 3 \times 10^4$ K, while the broad-line region (BLR) reprocesses 5 per cent of this radiation from a radius $R_{\rm BLR} \approx 0.05$ pc, typical for these disc luminosities. We also consider a dusty torus having extension $R_{\rm Torus} \approx 1$ pc that emits IR photons at blackbody temperature $T_{\rm Torus} \approx 100$ K with luminosity $L_{\rm T} \simeq L_{\rm d}$. Therefore, we consider an internal electron population *cI* in a jet region of longitudinal size $L \simeq 10^{17}$ cm and tangled magnetic field $B \simeq 1$ Gauss, moving with bulk Lorentz factor $\Gamma \simeq 18$ (see e.g. Tavecchio, Maraschi & Ghisellini 1998), in which the emission is due to synchrotron process and IC with the same synchrotron photons plus external photons coming from

Table 4. Model parameters for the AGN.

Ext. source	$L(10^{45}$ erg s$^{-1})$	T(K)	R(pc)
Accr. disc	1	3×10^4	$R_{\rm BLR} = 0.05$
Dusty torus	1	100	$R_{\rm Torus} = 1$

Table 5. Model parameters for the γ-ray flare F1.

Comp.	θ	B(G)	γ_b	ζ_1	ζ_2	$\gamma_{\rm max}$
cI	1.5	1	600	2.3	3.5	10^3
cII	1	0.2	500	2.1	3.5	3×10^3

the accretion disc, the BLR and the dusty torus. At the BLR edge, we assume that the cooled electrons of *cI* are re-accelerated to a *cII* component (of size $R \simeq 3 \times 10^{16}$ cm) by, for example, kink or tearing instability (Bodo et al. 2022) that slightly modifies the viewing angle θ. This second component accounts for the enhanced γ-ray flux via IC with the external soft photons. The magnetic field in *cII* is then assumed to decrease to 0.2 Gauss as the plasmoid moves away from the centre, towards the BLR edge. Moreover, we assume the emitters to have a jet-frame distribution of the random energies (γmc^2), starting from $\gamma_{\rm min} = 30$ (see e.g. Donnarumma et al. 2011), in the form of a standard broken power law

$$n_e(\gamma) = \frac{K\,\gamma_b^{-1}}{(\gamma/\gamma_b)^{\zeta_1} + (\gamma/\gamma_b)^{\zeta_2}}, \quad (5)$$

where ζ_1 and ζ_2 are the spectral indices for $\gamma < \gamma_b$ and $\gamma > \gamma_b$, respectively, γ_b is the Lorentz factor at the break and the normalization is assumed $K \simeq 1$ corresponding to an electron density $\sim$70 cm^{-3} for *cI* and $K \simeq 30$ corresponding to an electron density $\sim 10^3$ cm^{-3} for *cII*, respectively. Table 4 shows the parameters we assumed for PKS 1830-211, while Table 5 shows the values of the parameters for the two components, *cI* and *cII*, responsible for the overall SED. Assuming a bulk Lorentz factor $\Gamma \simeq 18$ and the values of the viewing angles θ reported in Table 5, we obtain Doppler factors of the order of 29–32 for *cI* and *cII*, respectively. These values are in agreement with the minimum Doppler factor derived in Section 3.1.

Fig. 8 shows the multicomponent fit to our data, as described above. The different lines represent different emission components. We note that the main contribution to the IC peak is provided by the inverse Compton off the BLR photons, as suggested by the achromatic behaviour reported in Fig. 6.

The Eddington luminosity is $L_{\rm Edd} \approx 6.2 \times 10^{46}$ erg s^{-1}, where we assumed the value of the black hole mass reported by Nair, Jin & Garrett (2005), $M_{\rm BH} = 5 \times 10^8$ M$_\odot$. The total power carried in the jet, $P_{\rm jet}$, can be calculated following Ghisellini & Celotti (2001) as

$$P_{\rm jet} = P_{\rm B} + P_{\rm p} + P_{\rm e} + P_{\rm rad}, \quad (6)$$

where $P_{\rm B}$, $P_{\rm p}$, $P_{\rm e}$, and $P_{\rm rad}^{\rm bol}$ are the power carried by the magnetic field, the cold protons, the relativistic electrons, and the produced radiation, respectively. In order to compute the different components, we use the formalism presented in Celotti & Ghisellini (2008). We obtain: $P_{\rm B} \approx 8 \times 10^{45}$ erg s^{-1}, $P_{\rm e} \approx 5 \times 10^{44}$ erg s^{-1}, $P_{\rm p} \approx 2 \times 10^{46}$ erg s^{-1},

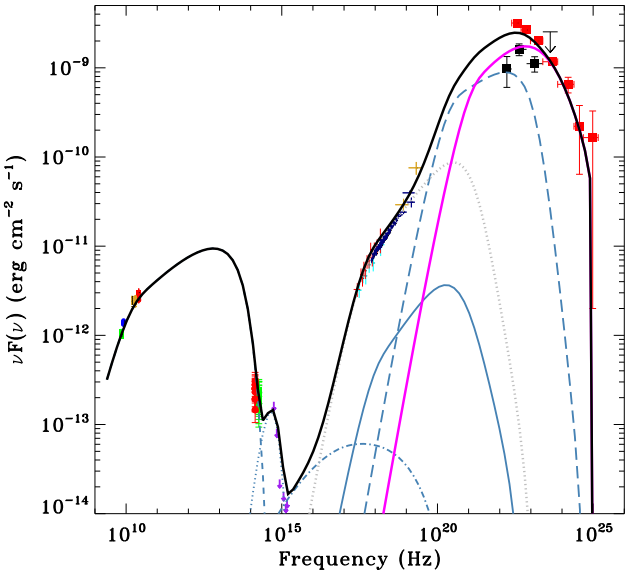

Figure 8. PKS 1830-211 SEDs for the flare F1 with different fit components. Data points follow the colour scheme adopted for Fig. 7. Different lines correspond to different spectral components. Blue dotted is the disc emission, blue dashed is the synchrotron emission, blue dashed–dotted is the synchrotron self-Compton emission, blue triple-dotted–dashed is external Compton off the disc photons emission, blue long-dashed is the external Compton off the BLR photons emission, grey dotted is the external Compton off the torus photons emission, magenta solid is the external Compton off the BLR photons emission of component *cII*, and black solid is the sum of all the different components.

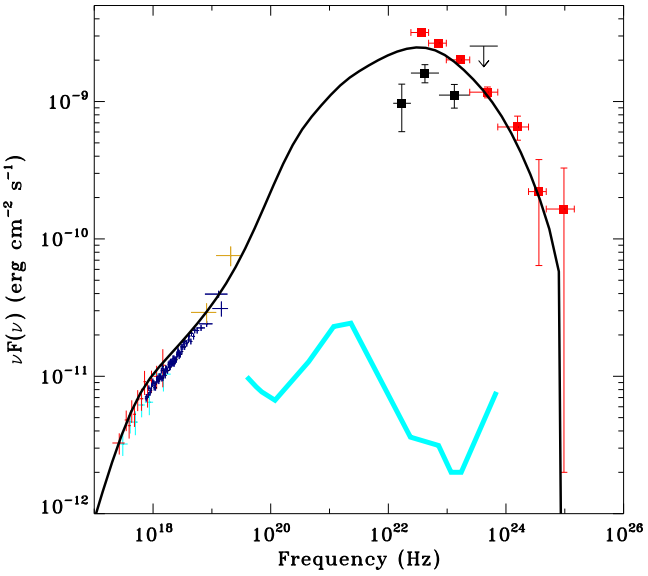

Figure 9. IC peak region of PKS 1830-211. Data points and the black solid line follow the colour scheme adopted for Fig. 7. The cyan curve represents the ASTROGAM sensitivity for an integration time of 6 d.

$P_{\rm rad} \approx 2.0 \times 10^{46}\,{\rm erg\,s^{-1}}$, which yields $P_{\rm jet} \approx 5 \times 10^{46}\,{\rm erg\,s^{-1}}$. This is comparable to the maximum $P_{\rm jet}$ value computed during the 2010 October flare in Donnarumma et al. (2011). We also note that, due to the high variability of PKS 1830-211, the comparison of model parameters is not always straightforward. While the γ-ray flare modelled in Donnarumma et al. (2011) is not dramatically different from the one discussed in this work, the SED discussed in De Rosa et al. (2005) reached a γ-ray peak more than two order of magnitude lower than the present one, since they reported the Third EGRET Catalogue (Hartman et al. 1999) spectrum. We also note that, despite a different definition of the different γ-ray flares and SED model parameters, our $P_{\rm jet}$ estimate is compatible with the one reported in Abhir et al. (2021).

3.3 Prospects for detection in the MeV and VHE bands

Fig. 9 shows the IC peak region of PKS 1830-211 data. The cyan curve represents the ASTROGAM sensitivity for an integration time of 6 d (see Vercellone et al. 2019, for further details). ASTROGAM is a proposed Observatory space mission dedicated to the study of the non-thermal Universe in the photon energy range from 0.3 MeV to 3 GeV (De Angelis et al. 2017, 2021). ASTROGAM could be a very useful mission in order to study high-redshift, powerful FSRQs such as PKS 1830-211 (Donnarumma et al. 2011, and this work), 4C +71.07 (Vercellone et al. 2019) and a small sample in Marcotulli et al. (2020). As seen in Fig. 9, ASTROGAM would sample the IC component, providing crucial data which cover the energy range from 0.1 MeV up to a few hundreds of MeV. This would allow us to cover a currently unsampled energy range, and to obtain important data to constrain the IC peak in high-z FSRQs.

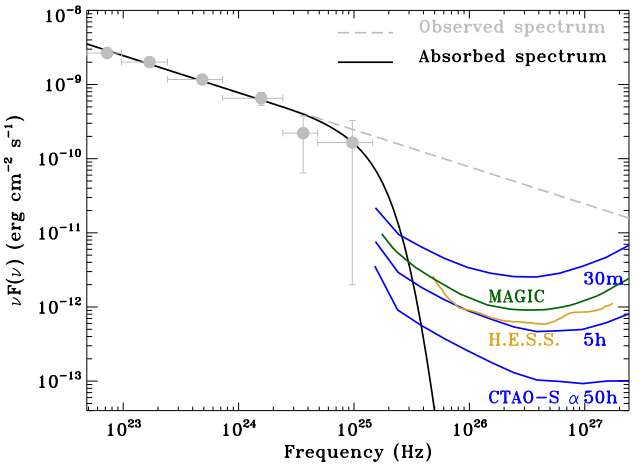

Figure 10. Grey data and dashed lines represent the *Fermi*-LAT data and power-law spectrum during flare F1, while the black solid line represent the EBL-absorbed PKS 1830-211 spectrum at energies above 10 GeV. Green and golden lines represent the MAGIC and H.E.S.S.-I differential sensitivity curves for and integration time of 50 h, respectively. Blue lines represent the CTAO-S Alpha Configuration differential sensitivity curves for different integration times (0.5, 5, and 50) h (see https://www.cta-observatory.org/science/ctao-performance/).

Fig. 10 shows the *Fermi*-LAT data and power-law spectrum during flare F1, extrapolated to higher energies, in the optimistic assumption that no intrinsic cut-off applies. The correction for absorption by the extragalactic background light (EBL), providing substantial attenuation only above a few tens of GeV, has been applied using the model of Domínguez et al. (2011, black solid line). We note that during a previous PKS 1830-211 γ-ray flare that occurred on 2014 July 27 (Krauss et al. 2014), the source was also observed by the H.E.S.S.-II array, starting about 20 d after the *Fermi*-LAT alert in order to investigate possible delayed emission at very high energies (H. E. S. S. Collaboration 2019). This observation was performed by adding the large CT5 telescope, which provides detection capabilities below

100 GeV (H. E. S. S. Collaboration 2017). No significant signal was detected above ∼67 GeV. The green, gold, and blue solid lines correspond to the MAGIC (50 h), H.E.S.S (50 h), and CTAO alpha configuration[1] (50, 5, and 0.5 h) differential sensitivity, respectively. MAGIC can observe PKS 1830 -211 at a Zenith angle of about 50°, which increases its low-energy threshold, while the H.E.S.S.-I sensitivity (when considering the usual CT1–4 configuration) does not extend significantly at energies lower than 100 GeV. CTAO, in its alpha configuration, might be able to detect PKS 1830- 211 with a short integration time (0.5–5) h up to 100 GeV. The detection of FSRQs by IACTs may challenge the current paradigm of the HE–VHE emission occurring within or at the edge of the BLR. As shown in Costamante et al. (2018), the γ-ray emission from *Fermi*-LAT FSRQs might be explained by means of emitting mechanisms which do not involve the jet interaction with the BLR. Moreover, evidence is emerging that for blazars the location of the γ-ray emitting region may not always be placed at the same distance from the central black hole during different flaring episodes of the same source as suggested by Brown (2013) for PKS 1510 − 089 or by Coogan, Brown & Chadwick (2016) and Finke (2016) for 3C 454.3. A few FSRQs have been already detected by current IACTs (see also http://tevcat.uchicago.edu/). Therefore, the detection of PKS 1830-211 by CTAO during particular strong flares could shed light on the location of the gamma-ray emitting zone and the related emission mechanisms.

4 SUMMARY AND CONCLUSIONS

In this paper, we presented the multiwavelength behaviour, from radio frequencies up to the γ-ray energy band, of the lensed quasar PKS 1830-211 during multiple flaring episodes that occurred in the period 2019 mid-February to mid-April through nearly simultaneous observations presented here for the first time. We can summarize our findings as follows:

(i) The *Fermi*-LAT data show three major γ-ray flares, F1 (MJD 58575.2–58576.1), F2 (MJD 58595.0–58598.8), and F3 (MJD 58601.5–58603.4), respectively. The minimum variability time-scale for $E > 100$ MeV is $t_{\rm var} = 0.15$ d, while it emerges there could be a slightly enhanced fractional variability when considering the lower energy threshold ($E > 100$ MeV) with respect to the higher one ($E > 300$ MeV). Moreover, we confirm the higher fractional variability in the γ-ray energy band with respect to the one at lower frequencies. Another interesting result is on γ-ray spectral variability as a function of the flux. As already noted for other sources (3C 454.3, Vercellone & Romano 2014, in the 0.2–10 keV energy band) there is a roughly achromatic increase of the γ-ray emission. This could be explained, for example, with the dominance of the external Compton emission mechanism in the γ-ray energy band.

(ii) X-ray data show moderate variability during the whole observing period. A detailed analysis of *Chandra* data show a hint of variability of the absorbing column density in the lensing galaxy.

(iii) Radio data show an interesting behaviour. Investigating the data in the frequency range 7–25.5 GHz, we find a spectral break above 15 GHz, with a decrease of the flux density at the highest frequency in the observed time range. Similar breaks in the radio spectra could be found in other extragalactic jetted sources, due to radio flux variability at different wavelengths in times. Moreover, 15 GHz data show a continuous flux rising up to a maximum occurring about 110 d after the γ-ray flares, suggesting possible different locations of the γ-ray and radio emission zones.

(iv) UV–optical data are challenging to be acquired. While we have only upper limits in the UV–optical wavebands, IR data show no particular variability pre-, during, and post-flare F1 episode.

(v) The SED modelling shows that our data are consistent with a multiple-component emission model, where the emission in the energy band above 100 MeV could be interpreted by the IC emission, at the edge of the BLR, of electrons re-accelerated by kink or tearing instability. Moreover, the total jet power is comparable to that of the 2010 flare.

(vi) Finally, PKS 1830-211 is an excellent candidate for upcoming both Compton and VHE facilities. Upcoming Compton missions will probe the IC peak in high-z FSRQs, while a possible detection of PKS 1830- 211 would increase the number of FSRQs detected at VHE and provide useful information of the location of the γ-ray emitting zone during different flares.

[1]The 'Alpha Configuration' for the southern CTAO array consists of 14 medium-sized telescopes and 37 small-sized telescopes. See https://www.cta-observatory.org/science/ctao-performance/ for further details.

ACKNOWLEDGEMENTS

SV, ID, CP, FC, AdR, LdG, SK, MNI, APP, EE, LP, GP, SP, SR, GV, FV, and VV contributed equally to this work. We thank the referee for the prompt reply and the valuable comments which improved the quality of the manuscript. The authors acknowledge financial contribution from the grant ASI I/028/12/0. SV acknowledges financial contribution from the agreement ASI–INAF no. 2017-14-H.0. The Sardinia Radio Telescope is funded by the Ministry of University and Research (MIUR), Italian Space Agency (ASI), and the Autonomous Region of Sardinia (RAS) and is operated as National Facility by the National Institute for Astrophysics (INAF). The Medicina radio telescope is funded by the Ministry of University and Research (MIUR) and is operated as National Facility by the National Institute for Astrophysics (INAF). This research has made use of data from the OVRO 40-m monitoring program (Richards et al. 2011), supported by private funding from the California Institute of Technology and the Max Planck Institute for Radio Astronomy, and by NASA grants NNX08AW31G, NNX11A043G, and NNX14AQ89G and NSF grants AST-0808050 and AST-1109911. SK acknowledges support from the European Research Council (ERC) under the European Unions Horizon 2020 research and innovation programme under grant agreement no. 771282. Part of this work is based on archival data, software or online services provided by the Space Science Data Center – ASI.

DATA AVAILABILITY

The data underlying this article are publicly available from the *Fermi*-LAT, AGILE-GRID, *INTEGRAL*, *NuSTAR*, *Chandra*, *Swift*, SRT/Medicina, and REM archives and processed with publicly available software (SRT/Medicina SDI software can be available upon request). OVRO 40-m data are available upon request to Sebastian Kiehlmann (skiehl@physics.uoc.gr).

REFERENCES

Abdo A. A. et al., 2010, ApJ, 710, 1271
Abdo A. A. et al., 2015, ApJ, 799, 143
Abdollahi S. et al., 2020, ApJS, 247, 33
Abhir J., Prince R., Joseph J., Bose D., Gupta N., 2021, ApJ, 915, 26
Angioni R., 2019, ATel, 12601 1
Araudo A. T., Bosch-Ramon V., Romero G. E., 2010, A&A, 522, A97

Atwood W. B. et al., 2009, ApJ, 697, 1071
Baars J. W. M., Genzel R., Pauliny-Toth I. I. K., Witzel A., 1977, A&A, 500, 135
Barnacka A., Geller M. J., Dell'Antonio I. P., Benbow W., 2015, ApJ, 809, 100
Blackburne J. A., Pooley D., Rappaport S., 2006, ApJ, 640, 569
Bodo G., Mamatsashvili G., Rossi P., Mignone A., 2022, MNRAS, 510, 2391
Breeveld A. A., Landsman W., Holland S. T., Roming P. , Kuin N. P. M., Page M. J., 2011, in AIP Conf. Proc. Vol. 1358, Gamma ray Bursts 2010. Am. Inst. Phys., New York, p. 373
Brown A. M., 2013, MNRAS, 431, 824
Bulgarelli A., Chen A. W., Tavani M., Gianotti F., Trifoglio M., Contessi T., 2012, A&A, 540, A79
Bulgarelli A. et al., 2014, ApJ, 781, 19
Bulgarelli A. et al., 2019, A&A, 627, A13
Burrows D. N. et al., 2005, Space Sci. Rev., 120, 165
Cardillo M. et al., 2019, ATel, 12622 1
Celotti A., Ghisellini G., 2008, MNRAS, 385, 283
Coogan R. T., Brown A. M., Chadwick P. M., 2016, MNRAS, 458, 354
Costamante L., Cutini S., Tosti G., Antolini E., Tramacere A., 2018, MNRAS, 477, 4749
Courbin F., Meylan G., Kneib J.-P., Lidman C., 2002, ApJ, 575, 95
Dai X., Mathur S., Chartas G., Nair S., Garmire G. P., 2008, AJ, 135, 333
De Angelis A. et al., 2017, Exp. Astron., 44, 25
De Angelis A. et al., 2021, Exp. Astron., 51, 1225
De Rosa A. et al., 2005, A&A, 438, 121
Dickey J. M., Lockman F. J., 1990, ARA&A, 28, 215
Domínguez A. et al., 2011, MNRAS, 410, 2556
Dondi L., Ghisellini G., 1995, MNRAS, 273, 583
Donnarumma I. et al., 2011, ApJ, 736, L30
Egron E. et al., 2017a, MNRAS, 470, 1329
Egron E. et al., 2017b, MNRAS, 471, 2703
Feroci M. et al., 2007, Nucl. Instr. Meth. Phys. Res. A, 581, 728
Finke J. D., 2016, ApJ, 830, 94
Fitzpatrick E. L., 1999, PASP, 111, 63
Fromm C. M. et al., 2011, A&A, 531, A95
Gehrels N. et al., 2004, ApJ, 611, 1005
Ghisellini G., Celotti A., 2001, MNRAS, 327, 739
Ghisellini G., Maraschi L., Treves A., 1985, A&A, 146, 204
Glaz J., Zhang Z., 2006, Stat. Probab. Lett., 76, 1316
Goldwurm A. et al., 2003, A&A, 411, L223
H. E. S. S. Collaboration, 2017, A&A, 600, A89
H. E. S. S. Collaboration, 2019, MNRAS, 486, 3886
Harrison F. A. et al., 2013, ApJ, 770, 103
Hartman R. C. et al., 1999, ApJS, 123, 79
Iacolina M. N. et al., 2019, ATel, 12667, 1
Krauss F., Becerra J., Carpenter B., Ojha R., Buson S., 2014, ATel, 6361, 1
Labanti C. et al., 2009, Nucl. Instr. Meth. Phys. Res. A, 598, 470
Lidman C., Courbin F., Meylan G., Broadhurst T., Frye B., Welch W. J. W., 1999, ApJ, 514, L57
Loru S. et al., 2019, MNRAS, 482, 3857
Lovell J. E. J., Jauncey D. L., Reynolds J. E., Wieringa M. H., King E. A., Tzioumis A. K., McCulloch P. M., Edwards P. G., 1998, ApJ, 508, L51
Lucarelli F. et al., 2019, ATel, 12541 1
Marcotulli L. et al., 2020, ApJ, 889, 164
Mattox J. R. et al., 1996, ApJ, 461, 396
Mattox J. R., Schachter J., Molnar L., Hartman R. C., Patnaik A. R., 1997, ApJ, 481, 95
Melis A. et al., 2018, J. Astron. Instr., 7, 1850004
Nair S., Jin C., Garrett M. A., 2005, MNRAS, 362, 1157
Pacciani L., 2018, A&A, 615, A56
Perotti F., Fiorini M., Incorvaia S., Mattaini E., Sant'Ambrogio E., 2006, Nucl. Instr. Meth. Phys. Res. A, 556, 228
Pittori C., 2013, Nucl. Phys. B Proc. Suppl., 239, 104
Pittori C., The Agile-Ssdc Team, 2019, Rendiconti Lincei. Scienze Fisiche e Naturali, 30, 217
Pittori C. et al., 2019a, ATel, 12594, 1
Pittori C. et al., 2019b, ATel, 12603, 1
Planck Collaboration VI, 2020, A&A, 641, A6
Prest M., Barbiellini G., Bordignon G., Fedel G., Liello F., Longo F., Pontoni C., Vallazza E., 2003, Nucl. Instr. Meth. Phys. Res. A, 501, 280
Pushkarev A. B., Kovalev Y. Y., Lister M. L., 2010, ApJ, 722, L7
Readhead A. C. S., Lawrence C. R., Myers S. T., Sargent W. L. W., Hardebeck H. E., Moffet A. T., 1989, ApJ, 346, 566
Richards J. L. et al., 2011, ApJS, 194, 29
Schlafly E. F., Finkbeiner D. P., 2011, ApJ, 737, 103
Schleicher B. et al., 2019, Galaxies, 7, 62
Stratta G., Capalbi M., Giommi P., Primavera R., Cutini S., Gasparrini D., on behalf of the ASDC team, 2011, preprint (arXiv:1103.0749)
Tavani M. et al., 2009, A&A, 502, 995
Tavani M., Vittorini V., Cavaliere A., 2015, ApJ, 814, 51
Tavecchio F., Maraschi L., Ghisellini G., 1998, ApJ, 509, 608
Ubertini P. et al., 2003, A&A, 411, L131
Vaughan S., Edelson R., Warwick R. S., Uttley P., 2003, MNRAS, 345, 1271
Vercellone S., Romano P., 2014, in Proceedings of Swift: 10 Years of Discovery (SWIFT 10), Proceeeding of Science, SISSA Trieste, p. 167
Vercellone S. et al., 2010, ApJ, 712, 405
Vercellone S. et al., 2019, A&A, 621, A82
Verrecchia F. et al., 2013, A&A, 558, A137
Vitali F. et al., 2003, in Iye M., Moorwood A. F. M., eds, Proc. SPIE Conf. Ser. Vol. 4841, Instrument Design and Performance for Optical/Infrared Ground-based Telescopes. SPIE, Bellingham, p. 627
Vittorini V. et al., 2009, ApJ, 706, 1433
Vittorini V., Tavani M., Cavaliere A., Striani E., Vercellone S., 2014, ApJ, 793, 98
Vittorini V., Tavani M., Cavaliere A., 2017, ApJ, 843, L23
Wiklind T., Combes F., 1996, Nature, 379, 139
Wilms J., Buson S., Gokus A., Cheung T. C., Nowak M. A., Ciprini S., 2019, ATel, 12737, 1
Winkler C., 1994, ApJS, 92, 327
Zerbi F. M. et al., 2004, in Moorwood A. F. M., Iye M., eds, Proc. SPIE Conf. Ser. Vol. 5492, Ground-based Instrumentation for Astronomy. SPIE, Bellingham, p. 1590

APPENDIX A: GAMMA-RAY OBSERVATIONS

A1 AGILE data

The AGILE satellite (Tavani et al. 2009) is a mission of the Italian Space Agency (ASI) devoted to high-energy astrophysics. The AGILE scientific instrument combines four active detectors yielding broad-band coverage from hard X- to γ-ray energies: a Silicon Tracker (ST; Prest et al. 2003, 30 MeV–50 GeV), a co-aligned coded-mask hard X-ray imager, Super–AGILE (SA; Feroci et al. 2007, 18–60 keV), a non-imaging CsI Mini–Calorimeter (MCAL; Labanti et al. 2009, 0.3–100 MeV), and a segmented Anti-Coincidence System (ACS; Perotti et al. 2006). Any γ-ray detection is obtained by the combination of ST, MCAL, and ACS; these three detectors form the AGILE-GRID. A ground segment alert system allows the AGILE team to perform the full AGILE-GRID data reduction and the preliminary quick-look scientific analysis (Pittori 2013; Bulgarelli et al. 2014; Pittori & The Agile-Ssdc Team 2019).

PKS 1830-211 underwent an exceptionally bright active phase in γ-rays which started at the end of 2019 February and lasted approximately 2 months, as preliminarily reported in Lucarelli et al. (2019), Pittori et al. (2019a, b), Angioni (2019), and Cardillo et al. (2019). We carried out the analysis of the AGILE-GRID consolidated data (archive `ASDCSTDk`) above 100 MeV with the new `Build_25` scientific software, `FM3.119` calibrated filter, `H0025` response

matrices. We applied South Atlantic Anomaly event cuts and 80° Earth albedo filtering. Only incoming γ-ray events with an off-axis angle lower than 60° were selected for the analysis. Statistical significance and flux determination of the point sources were calculated using the AGILE multisource likelihood analysis software (MSLA; Bulgarelli et al. 2012) based on the Test Statistic (TS) method as formulated by Mattox et al. (1996). This statistical approach provides a detection significance assessment of a γ-ray source by comparing maximum-likelihood values of the null hypothesis (no source in the model) with the alternative hypothesis (point source in the field model).

We analysed the γ-ray data above 100 MeV between 2019 February 16 and May 29 (MJD: 58530–58632). We analysed eight statistically independent light curves with a 48-h time bin, with an MSLA approach by calculating the flux at the nominal position of the blazar. Each light curve is shifted by 6 h with respect to the previous one, in order to better describe the time evolution of the γ-ray emission and preserving the photon statistics of a single 48 h bin. In the multisource analysis, we took into account the emission of the nearby sources within a radius of analysis of 10°. Position and fluxes of the field sources have been kept fixed at the values of the Second AGILE Catalogue (Bulgarelli et al. 2019). The parameter quantifying the Galactic diffuse emission has been kept fixed at a standard value for an extragalactic source. The parameter related to the isotropic diffuse emission has been kept free to vary. Fig. A1 shows one of the eight independent light curves analysed in our study, namely the one whose temporal bins are in agreement with the *Fermi*-LAT ones.

In Fig. A2 and Table A1, we present the AGILE-GRID photon index versus the $E > 100$ MeV flux, related to the main relative γ-ray peaks, emerging from the overall time evolution of the emission from the blazar (8 time-shifted light curves). The photon indices have been calculated with a binned analysis in the energy band 100 MeV–3 GeV. Each flux has been calculated by keeping the correspondent spectral index fixed. No particular conclusions can be drawn on the correlation between the γ-ray flux and the photon index because of the too small number of data points (Spearman's coefficient $\rho = -0.89$ and $p \simeq 0.02$).

A2 *Fermi*-LAT data

We analysed the *Fermi*-LAT (Atwood et al. 2009) data using the standard tools provided with the SCIENCETOOLS version `v11r05p02`, and the instrument response functions `P8R3_SOURCE_V2` to produce light curves and spectra. We selected events within a region of 20° around the source nominal position, with reconstructed energy in the 0.1–300 GeV range. We filtered out γ-rays with zenith angles larger than 90° to reduce Earth limb γ-rays. We used the unbinned likelihood procedure to extract fluxes in energy and time bins. We modelled background using standard templates for isotropic and galactic diffuse background, and we included pointlike and diffuse sources from the fourth *Fermi*-LAT catalogue (Abdollahi et al. 2020) inside the region of interest. Figs A3 and A4 show the *Fermi*-LAT 12-h bin light curve obtained using likelihood standard analysis ($E > 100$ MeV) and the 12-h bin ($E > 300$ MeV) photon index versus 12-h bin flux, respectively. We note that the ($E > 300$ MeV) energy range used for the calculation of the spectral index is a conservative choice. The *Fermi*-LAT light curves were calculated for both $E > 100$ and > 300 MeV, the former to allow a proper comparison with the AGILE-GRID one.

Table A1. AGILE-GRID fluxes and photon indices at different relevant epochs.

Time interval (MJD)	$F(E > 100\,\mathrm{MeV})$ (photons cm^{-2} s^{-1})	Photon index
58561.25–58563.25	$(8.1 \pm 1.2) \times 10^{-6}$	2.28 ± 0.17
58566.50–58568.50	$(6.5 \pm 1.1) \times 10^{-6}$	2.35 ± 0.20
58574.75–58576.75	$(1.2 \pm 0.1) \times 10^{-5}$	2.32 ± 0.15
58581.75–58583.75	$(1.4 \pm 0.2) \times 10^{-5}$	2.20 ± 0.14
58587.75–58589.75	$(1.7 \pm 0.2) \times 10^{-5}$	2.03 ± 0.16
58596.25–58598.25	$(2.2 \pm 0.2) \times 10^{-5}$	2.16 ± 0.13

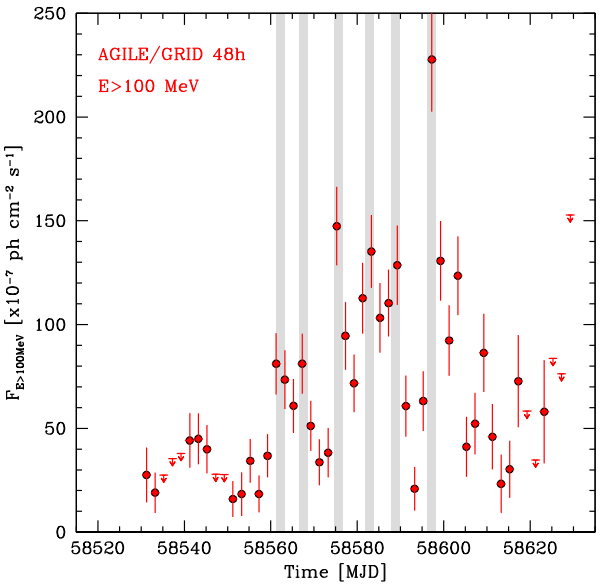

Figure A1. One of the eight statistically independent AGILE-GRID 48-h bin light curves ($E > 100$ MeV) analysed in our study, showing the maximum peak flux at MJD 58597.25 ± 1.0. Grey vertical bands correspond to the six high activity levels reported in Table A1.

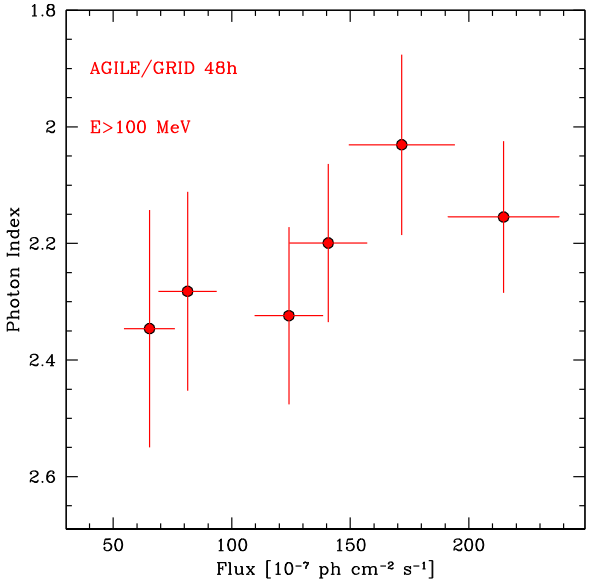

Figure A2. AGILE-GRID photon index versus the $E > 100$ MeV flux. See also Table A1.

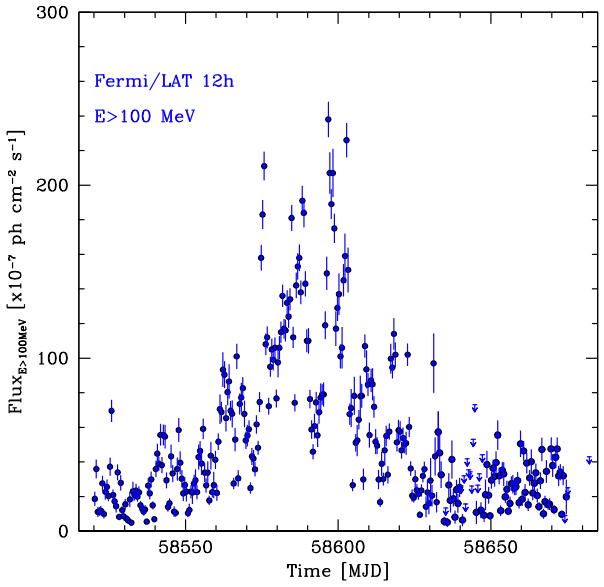

Figure A3. *Fermi*-LAT 12-h bin light curve obtained using likelihood standard analysis ($E > 100$ MeV) from 2019 February 06 to May 29.

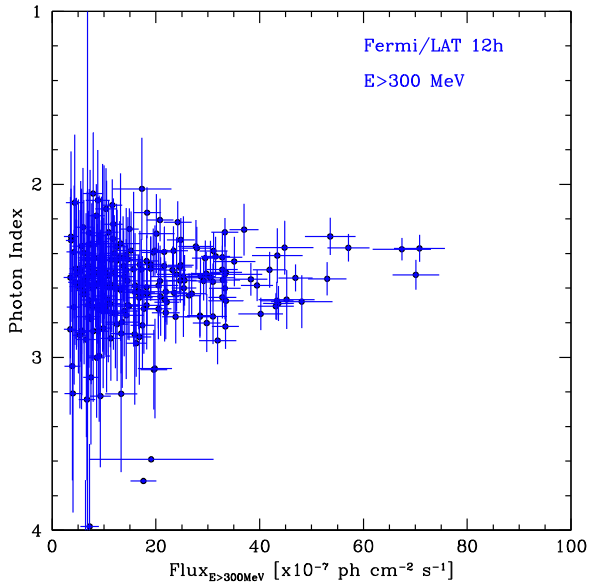

Figure A4. *Fermi*-LAT 12-h bin ($E > 300$ MeV) photon index versus 12-h bin flux from 2019 October 14 to May 20.

APPENDIX B: X–RAY OBSERVATIONS

Table B1 summarizes all the X-ray/hard X-ray observations, including *INTEGRAL*, *Swift*-XRT, *Chandra*, and *NuSTAR*.

B1 *INTEGRAL* data

The *INTEGRAL* (Winkler 1994) data set consists of a 180 ks public target of opportunity (ToO) observations performed from 2019 April 03 until 05 plus 13 ks of public General Program, in which the source was in partially coded field of view, performed on 2019 April 19. The *INTEGRAL* data reduction of the low-energy detector, ISGRI of γ-ray telescope IBIS (Ubertini et al. 2003) was performed using the standard Offline Scientific Analysis (OSA, Goldwurm et al. 2003) version 10.2 and the latest response matrices available. The source has been detected in the total ISGRI mosaic image (193 ks) at 7.1σ and 7.2σ level in the 15–30 and 30–200 keV energy ranges, respectively. The 20–50 keV ISGRI flux is 0.47 $\pm$ 0.07 counts s^{-1} (2.5×10^{-11} erg cm^{-2} s^{-1} or 4.4 mCrab). The 50–150 keV ISGRI flux is 0.55 $\pm$ 0.07 counts s^{-1} (7.9×10^{-11} erg cm^{-2} s^{-1} or

Table B1. Log of X-ray observations. MJDs are rounded for sake of simplicity. Actual MJD values can be derived from the ID column.

Date (MJD)	Satellite	ID	Duration (ks)
58545	*Swift*-XRT	00038422035	2.0
58548	*Swift*-XRT	00038422036	2.0
58550	*NuSTAR*	804606280002	40
58551	*Swift*-XRT	00038422037	1.9
58554	*Swift*-XRT	00038422038	2.0
58558	*Swift*-XRT	00038422039	1.9
58560	Swift-XRT	00038422040	1.7
58563	*Swift*-XRT	00038422041	2.1
58566	*Swift*-XRT	00038422042	2.0
58567	*Swift*-XRT	00038422044	1.8
58568	*Swift*-XRT	00038422045	2.0
58572	*Swift*-XRT	00038422047	1.8
58576	*Swift*-XRT	00038422049	0.8
58576	*INTEGRAL* (17 SCW)	16700030001	–
58577	*INTEGRAL* (15 SCW)	16700030001	–
58578	*Swift*-XRT	00038422050	1.6
58578	*INTEGRAL* (9 SCW)	16700030001	–
58581	*Swift*-XRT	00038422051	2.0
58583	*Swift*-XRT	00038422053	1.6
58584	*Swift*-XRT	00038422054	2.2
58585	*Swift*-XRT	00038422055	1.6
58587	*Swift*-XRT	00038422056	2.0
58590	*Swift*-XRT	00038422057	1.9
58592	*Chandra*	22197	15
58592	*INTEGRAL* (6 SCW)	16200150003	–
58593	*Swift*-XRT	00038422058	1.9
58600	*Swift*-XRT	00038422059	0.01
58602	*Swift*-XRT	00038422060	1.5
58602	*Swift*-XRT	00038422061	0.4
58606	*Swift*-XRT	00038422062	2.3
58608	*INTEGRAL* (1 SCW)	16200150003	–
56609	*Swift*-XRT	00038422063	2.0
58610	*Chandra*	22198	20
58615	*Swift*-XRT	00038422064	2.6
58618	*Swift*-XRT	00038422065	2.9
58621	*Swift*-XRT	00038422066	2.3
58627	*Swift*-XRT	00038422067	2.9
58627	Chandra	22199	25
58630	*Swift*-XRT	00038422068	2.6
58633	*Swift*-XRT	00038422069	1.4
58636	*Swift*-XRT	00038422070	3.3
58639	*Swift*-XRT	00038422071	0.2
58642	*Swift*-XRT	00038422072	2.7
58645	Swift-XRT	00038422073	2.2
58649	*Chandra*	22239	10
58650	*Chandra*	22240	10
58654	*Swift*-XRT	00038422074	1.5
58658	*Swift*-XRT	00038422075	0.3
58660	*Swift*-XRT	00038422076	1.1
58665	*Swift*-XRT	00038422077	1.1

Table B2. *Chandra* observation log.

Obs. ID	Date dd/mm/yyyy	Duration[a]	Observed flux[b] $F_{0.5-2.0\rm keV}$	$F_{2.0-10.0\rm keV}$
22197	19/04/2019	15	0.11 ± 0.03	1.3 ± 0.4
22198	07/05/2019	20	0.15 ± 0.03	1.6 ± 0.3
22199	24/05/2019	25	0.11 ± 0.02	1.3 ± 0.2
22239	15/06/2019	10	0.12 ± 0.03	1.4 ± 0.3
22240	16/06/2019	10	0.12 ± 0.03	1.4 ± 0.3

[a] Total duration of the observation in ks.
[b] Observed flux in the quoted bands. Units of 10^{-11} erg s^{-1} cm^{-2}.

10 mCrab). The ISGRI 20–50 keV flux increased during the ToO observation by about 17 per cent with respect to the averaged ISGRI flux reported in Donnarumma et al. (2011), while the 40–100 keV flux increment was of about 51 per cent, which is consistent with a hardening of the source spectrum. We extracted the PKS 1830-211 ISGRI averaged spectrum (13–200 keV) using both the standard OSA spectral extraction and the alternative procedure to extract a faint source spectrum (see OSA user manual for details.)[2] The resulting spectra were consistent. The best-fitting model consists in a simple power law with the photon index $\Gamma = 1.0 \pm 0.3$ and normalization $N_0 = 6.6^{+13}_{-2.1} \times 10^{-4}$ photons keV^{-1} cm^{-2} s^{-1} at 1 keV ($\chi^2_{\rm red} = 1.0$; 4 d.o.f.).

B2 *Swift*-XRT data

The *Neil Gehrels Swift* Observatory (*Swift* hereafter, Gehrels et al. 2004) data (Target ID 38422) were collected by activating two dedicated ToO observations triggered as a follow-up to AGILE detections. The XRT (Burrows et al. 2005, on-board *Swift*) event files were processed using the XRTDAS software package (v.3.6.0) developed at SSDC and distributed by the High Energy Astrophysics Science Archive Research Center (HEASARC) within the HEASOFT package. Calibrated and cleaned event files were produced using the calibration files in the *Swift*-XRT CALDB (20200724) and standard filtering criteria with the `xrtpipeline` task. We used the `xrtproducts` task included in the XRTDAS PACKAGE to extract the *Swift*-XRT source and background spectra using the appropriate response and ancillary files. We extracted spectra and light curves using circular apertures of radius 30 arcsec, centred on the peak of the emission in the 0.3–10 keV data. Background spectra were extracted using source-free annular regions of the 80/120 pixel inner/outer radius.

Fig. B1 shows the *Swift*/XRT photon index as function of the 0.3–10 keV observed flux. A possible harder-when-brighter trend is present (Spearman's coefficient $\rho = -0.31$ and $p < 0.009$).

B3 *Chandra* data

Chandra (Winkler 1994) pointed at PKS 1830-211 on discretionary director time observations. Five observations were acquired, three in 2019 April and May and two in 2019 June. Table B2 shows the log of the *Chandra* observations. We reprocessed the *Chandra* data using the '*Chandra* Interactive Analysis of Observations' (CIAO) package. For each observation, we created the clean level-2 event file using the `chandra_repro` script. De Rosa et al. (2005) reported that *Chandra* can resolve the two lensed images of PKS 1830-211 at an angular distance of the order of 1 arcsec. In order to search for possible spectral differences of the two hotspots (see below), we first align the WCS grid of all observations to the same reference coordinate. We follow the standard CIAO thread for absolute astrometric correction. For all observations, we use the `wcs_match` tool to compute the offset between the observed centroid and the reference coordinates. Hence, this can be input in `wcs_update` script to update the WCS grid of all the event files to match the reference coordinates (i.e. the coordinates of the source as observed in the first observation).

For all observations, we extracted the spectrum of PKS 1830-211 from a circular region with a radius of 4 arcsec. We took the background from an annular region, centred on the source, and with inner and outer radii of 20 and 25 arcsec, respectively. We fitted the spectra using XSPEC V12. It was already reported that PKS 1830-211 displays a highly absorbed spectrum, with the absorption arising in the intervening lensing galaxy at $z = 0.89$. Thus, we fitted all the spectra with a model that included the Galactic absorption ($N_{\rm H}^{\rm gal} = 2.19 \times 10^{21}$ cm^{-2}, Dickey & Lockman 1990), the absorption at the redshift of the lensing galaxy, and a power-law continuum. The free parameters of the fits are the intervening column density, $N_{\rm H}^{\rm lens}$, the photon index, and the normalization of the power law. Fig. B3 shows the time evolution of the free parameters of our fits, observation by observation, while the observed fluxes measured from our spectral fitting are reported in Table B2. In all the *Chandra* observations, the global X-ray spectrum of PKS 1830-211 remained substantially stable, both in flux and in spectral shape.

B4 *NuSTAR* data

NuSTAR (Harrison et al. 2013) consists of two focal plane modules, FPMA and FPMB, is sensitive at 3–78.4 keV and has a field of view of 10 arcmin at 10 keV (Harrison et al. 2013). *NuSTAR* has a 18 arcsec FWHM (full width at half-maximum) with a half-power diameter of 58 arcsec. We analysed the *NuSTAR* observation of PKS 1830-211 performed in 2019 March. The observation log is given in Table B3.

The raw event files were processed using the *NuSTAR* Data Analysis Software package v. 2.0.0. NUSTARDAS.[3] Calibrated and cleaned event files were produced using the calibration files in the *NuSTAR* CALDB (20200813) and standard filtering criteria with the `nupipeline` task. We used `nuproducts` task included in the NUSTARDAS package to extract the *NuSTAR* source and background spectra using the appropriate response and ancillary files. We extracted spectra and light curves in each focal plane module (FPMA and FPMB) using circular apertures of radius 90 arcsec, corresponding to ~ 90 per cent of the encircled energy, centred on the peak of the emission in the 3–78.4 keV data. Background spectra were extracted using source-free regions on the same detector as the source. As shown in Table B3, the background count rates are a small fraction (~ 6 per cent) of the source count rates. The spectra were binned to have at least 30 counts per bin.

[2] https://www.isdc.unige.ch/integral/download/osa/doc/11.1/osa_um_ibis.pdf

[3] http://heasarc.gsfc.nasa.gov/docs/nustar/analysis/nustar_swguide.pdf

Table B3. *NuSTAR* observation log.

Observation ID[a]	RA_PNT[b] (°)	DEC_PNT[c] (°)	Exposure[d] (ks)	Start date[e]	Rate[f] (counts s^{-1})	Background[g]
80460628002	278.4356	−21.0336	41.4	2019-03-08T20:21:09	0.458 ± 0.004	∼6 per cent

Notes. [a]Observation identification number. [b]Right ascension of the pointing. [c]Declination of the pointing. [d]Total net exposure time. [e]Start date and time of the observation. [f]Mean value of the net count rate in the circular source extraction region with 90 arcsec radius in the energy range 3–78.4 keV. [g]Background percentage in the circular source extraction region with 90 arcsce radius and in the energy range 3–78.4 keV.

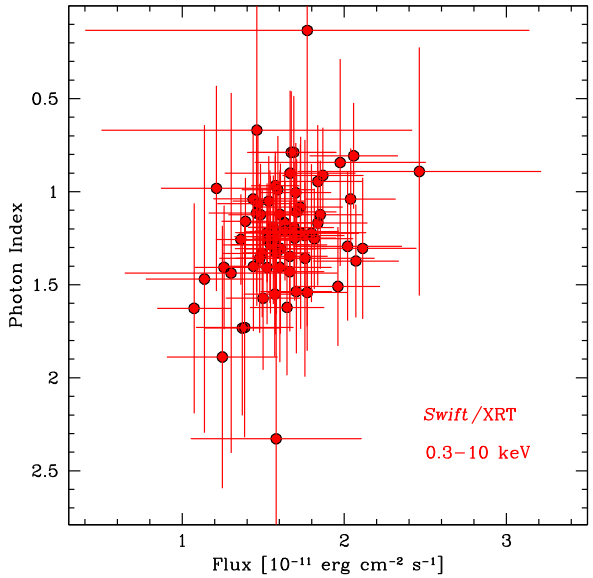

Figure B1. *Swift*/XRT photon index s a function of the 0.3–10 keV observed flux.

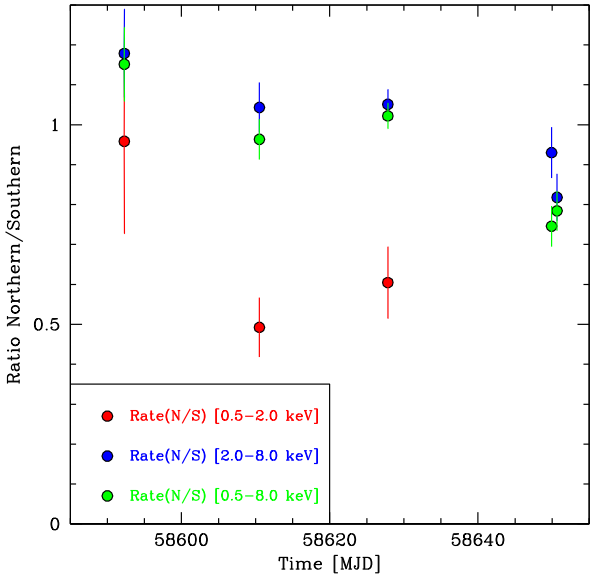

Figure B2. Ratios between the count-rate measured in the north and south hotspot of PKS 1830-211 as a function of time in the 0.5–2.0 (red), 2.0–8.0 (blue), and 0.5–8.0 keV (green) energy range.

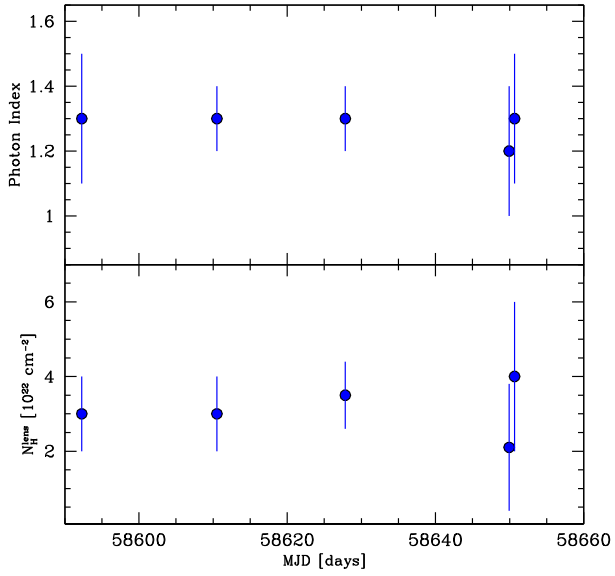

Figure B3. Time evolution of the parameters of the *Chandra* spectra. Upper panel: photon index. Lower panel: absorbing column density at the redshift of the lensing galaxy.

APPENDIX C: IR–OPTICAL–UV OBSERVATIONS

C1 *Swift*/UVOT data

The *Swift*/UVOT data were accumulated during the whole observing campaign, in order to establish the most reliable upper limits in the v, b, u, $w1$, $m2$, and $w2$ filters. Data were processed with HEASOFT V6.23 and CALDB (20201026). Due to the crowded field, particularly in optical bands, some nearby stars could contaminate an aperture of standard radius (see Fig. C1). To extract source counts we used a non-standard aperture of radius equal to the PSF FWHM, 2.2 arcsec, and three uncontaminated circular regions for the background extraction. We extracted source fluxes in each filter image available in each observation and on the sum of all the available images during the 2019 flaring campaign in each filter. No detections were obtained in any band, so we could not confirm the detection reported in Abhir et al. (2021). Observed magnitudes were converted into dereddened fluxes according to the CALDB conversion factors (Breeveld et al. 2011) and a mean Galactic extinction law (Fitzpatrick 1999) and $E(B-V)$ value of 0.397 (Schlafly & Finkbeiner 2011). Flux ULs on the summed images are reported in Table C1.

C2 REM data

The IR J, H, and K data have been obtained with the REMIR camera (Vitali et al. 2003), at the focal plane of the REM telescope (Zerbi

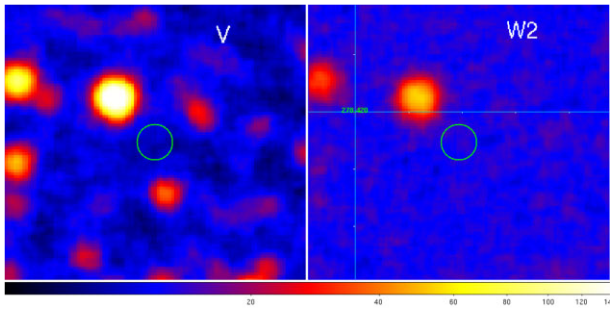

Figure C1. UVOT image for the *V* (left) and *W2* filters. The non-standard aperture of size 2.2 arcsec is shown in cyan colour.

Table C1. *Swift*/UVOT data.

Filter	Upper limits (dereddened) (erg s^{-1} cm^{-2})
v	$<1.80 \times 10^{-13}$
b	$<8.96 \times 10^{-14}$
u	$<2.42 \times 10^{-14}$
*w*1	$<1.74 \times 10^{-14}$
*m*2	$<1.29 \times 10^{-14}$
*w*2	$<1.45 \times 10^{-14}$

Table C2. REM IR data.

Time (MJD)	*H* filter (dereddened) (erg s^{-1} cm^{-2})	*K* filter (dereddened) (erg s^{-1} cm^{-2})
58565.0	$1.64 \times 10^{-13} \pm 6.19 \times 10^{-14}$	–
58566.0	$1.98 \times 10^{-13} \pm 7.45 \times 10^{-14}$	$2.54 \times 10^{-13} \pm 9.57 \times 10^{-14}$
58571.0	$2.17 \times 10^{-13} \pm 1.03 \times 10^{-13}$	$2.32 \times 10^{-13} \pm 8.73 \times 10^{-14}$
58573.0	$2.38 \times 10^{-13} \pm 6.65 \times 10^{-14}$	$2.79 \times 10^{-13} \pm 1.05 \times 10^{-13}$
58574.0	$2.17 \times 10^{-13} \pm 8.16 \times 10^{-14}$	$2.54 \times 10^{-13} \pm 7.11 \times 10^{-14}$
58577.0	–	$3.05 \times 10^{-13} \pm 5.66 \times 10^{-14}$
58578.0	$2.17 \times 10^{-13} \pm 6.06 \times 10^{-14}$	$2.79 \times 10^{-13} \pm 5.16 \times 10^{-14}$
58580.0	$2.38 \times 10^{-13} \pm 6.65 \times 10^{-14}$	$2.54 \times 10^{-13} \pm 4.71 \times 10^{-14}$
58584.0	$1.50 \times 10^{-13} \pm 5.65 \times 10^{-14}$	$1.46 \times 10^{-13} \pm 4.09 \times 10^{-14}$
58585.0	$1.80 \times 10^{-13} \pm 5.04 \times 10^{-14}$	$1.93 \times 10^{-13} \pm 5.39 \times 10^{-14}$
58586.0	–	$1.93 \times 10^{-13} \pm 5.39 \times 10^{-14}$

et al. 2004), in the ESO La Silla (Chile) observatory. Observations were carried out in 23 nights, in 2019 March and April, of which 12 were photometric. The NIR frames have been reduced with the semi-automatic pipeline RIACE (Giannini et al. in preparation), which performs the frames stack (to produce the science and sky frames), then uses the Two Micron All-Sky Survey (2MASS) stars in the field to calibrate the aperture photometry of the science target. Fig. 3 panel (b) shows the REM light curves for the *H* and *K* filters. Data are reported in Table C2.

APPENDIX D: RADIO OBSERVATIONS

D1 SRT/Medicina data

A radio observation campaign was undertaken with two INAF radio telescopes: the SRT[4] and the Medicina radio telescope.[5] The radio

[4]http://www.srt.inaf.it/
[5]http://www.med.ira.inaf.it/

Table D1. SRT and Medicina radio data.

Time (MJD)	7 GHz (Jy)	25.5 GHz (Jy)
	SRT times and data	
58596.253	15.8 ± 1.0	11.9 ± 0.8
58599.193	15.2 ± 1.0	11.7 ± 1.0
58601.226	14.5 ± 0.8	11.7 ± 1.5
58604.208	14.6 ± 0.9	11.5 ± 1.5
58607.184	14.0 ± 0.9	11.2 ± 1.0
58610.191	14.6 ± 0.8	11.3 ± 0.8
58613.190	15.2 ± 0.8	11.9 ± 1.3
58617.147	14.9 ± 1.0	11.6 ± 1.0
58626.113	15.4 ± 1.5	11.5 ± 0.5
58630.169	15.7 ± 1.0	10.5 ± 1.0
	Medicina times and data	
Time (MJD)	8.3 GHz (Jy)	25.5 GHz (Jy)
58590.228	16.0 ± 1.0	9.8 ± 0.9
58592.236	17.0 ± 1.0	11.8 ± 0.5
58644.900	16.0 ± 1.0	10.2 ± 0.5
58649.941	17.0 ± 0.5	10.7 ± 0.5
58651.925	17.0 ± 0.7	10.7 ± 0.9
58655.902	16.5 ± 0.4	9.7 ± 0.6
58659.902	17.1 ± 0.4	9.8 ± 0.6
58662.905	17.6 ± 0.5	10.7 ± 1.0

follow-up started on MJD 58590.2 and ended on MJD 58662.9. 18 dual-frequency observing sessions were performed: 8 with Medicina at 8.3 and 25.4 GHz using `total power` back end with 250 and 680 MHz bandwidth, respectively, and 10 sessions with the SRT at 7 and 25.5 GHz, where SARDARA back end (Melis et al. 2018) was used with a 1400 MHz bandwidth. Single-dish radio mapping techniques were exploited to perform On The Fly maps of the source and a sample of the best-known radio astronomical flux calibrators (3C 286, 3C 295, and NGC 7027). The follow-up was undertaken in the context of two INAF ToO programs and one Director Discretionary Time proposal. Preliminary results were published in Iacolina et al. (2019). Radio imaging data analysis and calibration were performed using the techniques explained in Egron et al. (2017b, a) and Loru et al. (2019), comparing counts of the Gaussian fit in the target image with calibrators images and cross-scans. Most of the radio data were of good quality. However, the low elevation of the source, bad weather (fog and rain), and strong radio frequency interference (RFI) affected the data scans (i.e. enhanced and variable error bars in flux densities). Fig. 3, panel (a), shows the multifrequency radio flux density light curve (in Jy) obtained with SRT and Medicina radio telescopes in the MJD 58590.2−58662.9 period.

D2 OVRO data

The OVRO 40-Meter Telescope uses off-axis dual-beam optics and a cryogenic receiver with 2 GHz equivalent noise bandwidth centred at 15 GHz. Gain fluctuations, atmospheric and ground contributions are removed with the double-switching technique (Readhead et al. 1989) where the observations are conducted in an ON–ON fashion such that one of the beams is always pointed on the source. The two beams were rapidly alternated using a Dicke switch until 2014 May. In 2014 May, a new pseudo-correlation receiver with a 180° phase switch replaced the old receiver. To compensate for gain drifts relative calibration is obtained with a temperature-stable noise diode.

The primary flux density calibrator is 3C 286 with an assumed value of 3.44 Jy (Baars et al. 1977), DR21 is used as secondary calibrator source. Richards et al. (2011) give details about the observation procedure and data reduction. Fig. 3, panel (a), shows the OVRO radio flux density light curve (in Jy).

[1]*INAF, Osservatorio Astronomico di Brera, Via Emilio Bianchi 46, I-23807 Merate (LC), Italy*
[2]*ASI, Via del Politecnico, I-00133 Roma, Italy*
[3]*INAF, Osservatorio Astronomico di Roma, via Frascati 33, I-00078 Monte Porzio Catone, Italy*
[4]*ASI Space Science Data Center, Via del Politecnico, I-00133 Roma, Italy*
[5]*INAF, Istituto di Astrofisica e Planetologia Spaziali, Via Fosso del Cavaliere 100, I-00133 Roma, Italy*
[6]*Institute of Astrophysics, Foundation for Research and Technology-Hellas, GR-71110 Heraklion, Greece*
[7]*Department of Physics, University of Crete, GR-70013 Heraklion, Greece*
[8]*INAF, Osservatorio Astronomico di Cagliari, Via della Scienza 5, I-09047 Selargius (CA), Italy*
[9]*INAF, Istituto di Radioastronomia, via Piero Gobetti 93/2, I-40129 Bologna, Italy*
[10]*INAF, Osservatorio Astronomico d'Abruzzo, Via Mentore Maggini, I-64100 Teramo, Italy*
[11]*School of Physics, University of the Witwatersrand, 1 Jan Smuts Avenue, Braamfontein 2000 Johannesburg, South Africa*
[12]*Finnish Center for Astronomy with ESO (FINCA), University of Turku, FI-20014 Turku, Finland*
[13]*Aalto University Metsähovi Radio Observatory, Metsähovintie 114, FI-02540 Kylmälä, Finland*
[14]*Departamento de Astronomía, Universidad de Chile, Camino El Observatorio 1515, Las Condes, Santiago, Chile*
[15]*Owens Valley Radio Observatory, California Institute of Technology, Pasadena, CA 91125, USA*
[16]*Departamento de Astronomía, Universidad de Concepción, 4030000 Concepción, Chile*
[17]*INAF, Osservatorio di Astrofisica e Scienza dello Spazio, via Gobetti 101, I-40129 Bologna (BO), Italy*
[18]*INFN Sezione di Pavia, via U. Bassi 6, I-27100 Pavia (PV), Italy*
[19]*INFN Sezione di Roma Tor Vergata, Via della Ricerca Scientifica 1, I-00133 Roma, Italy*

This paper has been typeset from a TEX/LATEX file prepared by the author.